The published version of the paper "Erlantz Lizundia, Elena Fortunati, Franco Dominici, José Luis Vilas, Luis Manuel Leon, Ilaria Armentano, Luigi Torre, Jose M. Kenny (2016). PLLA-grafted cellulose nanocrystals: Role of the CNC content and grafting on the PLA bionanocomposite film properties Carbohydrate Polymers, 142, 105-113" is available at: https://doi.org/10.1016/j.carbpol.2016.01.041

PLLA-grafted cellulose nanocrystals: Role of the CNC content and grafting on the PLA bionanocomposite film properties

Erlantz Lizundia[a], Elena Fortunati[a,*], Franco Dominici[b], José Luis Vilas[a,c],

Luis Manuel Leon[a,c], Ilaria Armentano[b,*], Luigi Torre[b], Jose M. Kenny[b]

[a] Macromolecular Chemistry Research Group (LABQUIMAC), Department ofPhysical Chemistry, Faculty of Science and Technology,

University of the Basque Country (UPV/EHU), Leioa 48940, Spain

[b] University ofPerugia, Civil and Environmental Engineering Department, UdR INSTM, Strada di Pentima 4, 05100 Terni, Italy

[c] Basque Centerfor Materials, Applications and Nanostructures (BCMaterials), Parque Tecnologico cle Bizkaia, Ed. 500, Derio 48160, Spain

Abstract

Cellulose nanocrystals (CNC), extracted from microcrystalline cellulose by acid hydrolysis, were grafted by ring opening polymerization of l-Lactide initiated from the hydroxyl groups available at their sur-face and two different CNC:l-lactide ratios (20:80 and 5:95) were obtained. The resulting CNC-g-PLLA nanohybrids were incorporated in poly(lactic acid) (PLA) matrix by an optimized extrusion process at two different content (1 wt.% and 3 wt.%) and obtained bionanocomposite films were characterized by thermal, mechanical, optical and morphological properties. Thermal analysis showed CNC grafted with the higher ratio of lactide play a significant role as a nucleating agent. Moreover, they contribute to a significant increase in the crystallization rate of PLA, and the best efficiency was revealed with 3 wt.% of CNC-g-PLLA. This effect was confirmed by the increased in Young's modulus, suggesting the CNC graft ratio and content contribute significantly to the good dispersion in the matrix, positively affecting the final bionanocomposite properties.

1. Introduction

Polylactides (PLAs) have been known for several decades but only recently they have gained commercial significance as a leading environmentally benign plastic available from renewable resources (Armentano et

al., 2013). Besides of their bio-based character, they exhibit an excellent melt-processability, good biodegradability/biocompatibility, a room-temperature elastic modulus comparable to poly(ethylene terephthalate) and tunable crystallinity (Liu, Zhang, & Wang, 2014; Obarzanek-Fojt et al., 2014; Lizundia, Petisco, & Sarasua, 2013), which make them particularly interesting for the development of green materials (Auras & Selke, 2004). More precisely, the use of poly(lactic acid) in packaging applications would contribute to the reduction of the environmental impact associated with the massive use of traditional plastics based on petrochemical resources.

However, some of its functional properties still remain insufficient for their commercialization for food packaging and container applications. A possible solution to this matter may come from synergetic effect achieved when polymer matrices are mixed with nanoscale particles (Paul & Robeson, 2008; Armentano et al., 2013). In the aim of producing fully organic bionanocomposite based on poly(lactic acid) (PLA), cellulose nanocrystals (CNC) could be dispersed into PLA polymer matrix. CNC are large surface area nanoparticles based on cellulose, which represents the most abundant naturally available polymer on the Earth (Xiao, Gao, Lu, Li,Sun, 2015). The CNC properties make them ideal for mechanical reinforcing purposes. Dispersion and distribution of cellulose nanocrystals in a thermoplastic matrix is one of the most important issues in the development of CNC based high performance composites (Arias, Heuzey, Huneault, Ausias, & Bendahou, 2015). In this sense, when CNC are introduced within non-polar polymers such as PLA, they tend to bundle together due to the occurring intra- and inter-molecular hydrogen bonds between adjacent cellulose chains, which notably limits their efficiency as reinforcing elements (Dufresne, 2013). Furthermore, CNC show poor compatibility with hydrophobic polymer matrices because of the dominant hydrophilic nature of cellulose (Song, Xiao, & Zhao, 2014), which yields an inefficient transfer of CNC properties to its hosting matrix. Different strategies are available to solve this problem (Habibi, 2014; Lizundia, Vilas, & León, 2015b; Bitinis et al., 2013; Habibi, Aouadi, Raquez, & Dubois, 2013; Spinella et al., 2015; Fortunati et al., 2012a,b).

The chemical grafting of determined moieties on CNC sur-face would decrease the surface energy of the nanoparticle while increases the filler/matrix compatibility (Dufresne, 2013). Between all the techniques that are currently being employed, the poly-mer grafting known as “grafting from” strategy shows the brighter future. Taking advantage of the numerous surface hydroxyl groups of cellulose and the well-known ring-opening polymerization of polyesters (Dechy-Cabaret, Martin-Vaca, & Bourissou, 2004), surface-initiated ring opening polymerization (SI-ROP) emerges as the most suitable technique to overcome dispersion and com-patibility issues associated with the development of PLLA/CNC nanocomposites. This method presents the additional advantage of allowing the development of high grafting densities and con-trolled grafted chain lengths together with respecting the structural integrity of starting cellulose nanocrystals (Goffin et al., 2011). Another remarkable advantage of this method is that it permits the addition of dried CNC directly to the melt polymer, which rep-resents an almost essential requirement towards the development of solvent-free industrially-scalable fabrication process.

The goal of the present work consists of improving the inter-facial compatibility within CNC and hydrophobic PLA matrix in order to develop well dispersed and fully renewable bionanocom-posites film by using an industrial process technology. The role of the CNC grafting and its ratio and CNC-g-PLLA nanohybrid content added to the PLA, were investigated by a detailed investigation of physical and chemical properties of the obtained PLA based systems.

2. Materials and methods

2.1. Materials

L-lactide monomer (assay >99.5%) with <0.02% of water con-tent was provided by Purac Biochem (The Netherlands). Stannous octoate (Sn(Oct)2) and microcrystalline cellulose were supplied by Sigma Aldrich® . The chloroform and acetone were purchased from LabScan and utilized without further purification. Methanol was purchased by Panreac. Commercial poly(lactic acid) PLA 3251D, was purchased by NatureWorks® Co. LLC, USA. This PLA grade shows specific gravity 1.24 g/cm3 , and a melt flow rate (MFR) of 80 g/10 min tested at 210 ◦ C and 2.16 kg loading.

2.2. Cellulose nanocrystals synthesis and grafting

Cellulose nanocrystals (CNC) were obtained by sulfuric acid hydrolysis of microcrystalline cellulose as previously described (Lizundia et al., 2015b; Fortunati et al., 2012a,b). Grafting of PLLA from synthesized CNC has been performed by surface-initiated ring opening polymerization (SI-ROP) of l-lactide. Firstly, water-dispersed CNC were exchanged to toluene through sev-eral steps using acetone as an intermediate solvent as previously reported (Lizundia et al., 2015b). The CNC/toluene suspension was introduced into a three-neck flask immersed in a controlled tem-perature oil bath at 80 ◦ C. The required amount of previously dissolved L-lactide in toluene was poured into CNC suspension and (Sn(Oct)2) was added using a 100:1 monomer to catalyst ratio. Polymerization has been carried out for 24 h and was stopped by adding a few drops of diluted HCl solution. The resulting product was then precipitated in an excess of cold methanol and dried at 60 ◦ C under vacuum for 72 h. Obtained nanohybrids are termed as CNC-g-PLLA1 and CNC-g-PLLA2 for a CNC:l-lactide ratios of 20:80 and 5:95, which falls in the typical range utilized up to date (Goffin et al., 2011).

2.3. Characterization of CNC-g-PLLA nanohybrids

Cellulose nanocrystals were examined by transmission elec-tron microscopy (TEM) using a Philips CM120 Biofilter apparatus with STEM module at an acceleration voltage of 120 kV. A droplet of cellulose diluted water suspension (0.1% (w/w)) was deposited on hydrophilic carbon-coated grids and the specimens were neg-atively stained with 1% uranyl acetate (UO2(CH3COO)2) for 1 min and then observed using TEM. Infrared spectra in transmission KBr mode were recorded on a Thermo Nicolet Nexus 670 Fourier trans-

form infrared spectrophotometer (FT-IR). Samples were dried in vacuum at 60 ◦ C for 24 h before characterization. Each IR spectrum consisted of 64 scans taken in the range 600–4000 cm−1 with a resolution of 1 cm−1.

The thermal behavior of CNC-g-PLLA nanohybrids was deter-mined by using a Mettler Toledo DSC 822e calorimeter under nitrogen atmosphere (30 mL/min). Samples of 8 ± 1 mg were sealed in an aluminum pan, heated from -20 ◦ C to 170 ◦ C at a rate of 10 ◦ C/min in order to determine thermal transitions (Tg and Tm) and held at 170 ◦ C for 2 min so as to ensure that the previous thermal history is removed. After quenching the samples down to −20 ◦ C, a subsequent heating scan at 10 ◦ C/min was applied to the samples in order to determine the glass transition, cold crystallization and melting temperatures and enthalpies (Tg , Tcc , and Tm , Hcc , Hm). Thermal degradation behavior was studied by means of thermal gravimetric analysis (TGA METTLER TOLEDO 822e) in alumina pans with nitrogen flux of 50 mL/min for each sample (8 mg).

2.4. Characterization of CNC-g-PLLA nanohybrids

PLA and PLA based bionancomposites were processed and mixed by using a twin-screw microextruder (Dsm Explore 5&15 CC Micro Compounder). Processing parameters (screw speed, mix-ing time and temperature profile) were modulated to optimize the extrusion procedure. PLA pellets and CNC-g-PLLA nanohybrids were pre-dried to get rid of any moisture trace in the polymer structure and to avoid any undesirable hydrolysis reaction dur-ing processing. PLA was put into an oven at 98 ◦ C for 3 h, while CNC were dried overnight at 37 ◦ C. PLA and cellulose based films with thicknesses between 20 and 60 m were obtained with the adequate filmature die. Screw speed at 100 rpm was used to opti-mize the material final properties, while the temperature profile was set up at 180–195–210 ◦ C in the three different extrusion areas. The selected contents of CNC-g-PLLA (both CNC-g-PLLA1 and CNC-g-PLLA2) were 1 wt.% (designed PLA 1CNC-g-PLLA1 or PLA 1CNC-g-PLLA2) and 3 wt.% (designed as PLA 3CNC-g-PLLA1 or PLA 3CNC-g-PLLA2), in PLA polymer matrix.

2.5. PLA CNC-g-PLLA bionanocomposite characterization

2.5.1 Microstructure

The morphology and microstructure of the fracture surfaces of PLA and PLA bionanocomposite films were analyzed in a Hitachi S-4800 field emission scanning electron microscope (FESEM) at an acceleration voltage of 5 kV. Films were previously freeze-cut in liquid nitrogen, gold coated by an Emitech K550X sputter coater.

2.5.2. Optical absorption, gloss and color determination

The transparency of films was evaluated by visual observation and UV–vis optical absorption measurements, by using a Perkin Elmer Instruments (Lambda 35, USA) spectrophotometer, working in the wavelength between 250 and 900 nm. Color values were determined by using a spectrophotometer (CM-2300d Konica Minolta, Japan). Data were acquired by using a diffused illumination with a 8◦ viewing system (D/8 geometry) conforming to CIE N.15 and ISO 7724/1 standards. The measurement conditions were selected with the following standard parameters: observer at 10◦ (CIE 1964), illuminant D65 (Daylight, Color temperature 6504 K), while CIELAB colour variables, as defined by the Commission Internationale de 1 Éclairage (CIE, 1995), were used (CIE, 1995). Film specimens were placed on a white standard plate and L*, a*, and b* parameters were determined. Samples were evaluated per triplicate and three measurements were taken at random locations on each of the studied films. The total color difference E, between PLA and PLA bionanocomposite films was calculated as follows:

$$\Delta E = \sqrt{(\Delta L*)^2 + (\Delta a*)^2 + (\Delta b*)^2} \quad (1)$$

where L is the luminance component, which ranges from 0 to 100, and parameters a (from green to red) and b (from blue to yellow) are the two chromatic components, which range from −120 to 120, and L, a, and b are differences between each color value of the standard color plate and film specimen, respectively.

Gloss of PLA and PLA bionanocomposite films was determined considering the Specular Component Included with a diameter of the measurement area of 8 mm (SCI 8).

2.5.3. Thermal analysis

Differential scanning calorimetry (DSC-TA Instrument, Q200) measurements of PLA CNC-g-PLLA bionanocomposites were per-formed in the temperature range from −25 to 210 ◦ C at 10 ◦ C/min under nitrogen flow. PLA and PLA bionanocomposite samples (6–7 mg) were heated from −25 to 210 ◦ C at a rate of 10 ◦ C/min and held at 210 ◦ C for 2 min to erase the thermal history (1st scan), then they were cooled to −25 at 10 ◦ C/min (cooling) and reheated under the same conditions (2nd scan). Glass transition (Tg), cold crystallization (Tcc1 and Tcc2) and melting (Tm) temperatures and enthalpies (ΔHcc1, ΔHcc2, ΔHm) were determined from the first and second heating scans. The crystallinity degree (X) was calculated from the heating scans as:

$$\chi = \frac{\Delta H_m - \Delta H_{cc}}{\Delta H_0 \left(1 - m_f\right)} \times 100 \quad (2)$$

and from the cooling as:

$$\chi = \frac{\Delta H_c}{\Delta H_0 \left(1 - m_f\right)} \times 100 \quad (3)$$

where H0 is enthalpy of melting for a 100% crystalline PLA sample, taken as 93 J/g (Martin & Avérous, 2001), (1 − mf) is the weight fraction of PLA matrix in the sample, Hm and Hcc are the melting and cold crystallization enthalpies calculated from the first heating scan while the Hc is the crystallization enthalpy calculated from the cooling.

Thermodegradation products analysis has been performed by using a Fourier Transform Infrared Spectrophotometer (FT-IR) connected through an interface to DTG-60 Shimadzu thermobal-ance. Samples were heated from room temperature to 500 ◦ C at 10 ◦ C/min under nitrogen atmosphere. FT-IR scans were taken every 16 s.

2.5.4. Wide angle X-ray diffraction (WAXD)

The X-ray powder diffraction patterns were collected in a PHILIPS X'PERT PRO automatic diffractometer in theta-theta configuration, secondary monochromator with Cu-K radiation (= 1.5418 A)˚ and a PIXcel solid state detector. The sample was mounted on a zero background silicon wafer fixed in a generic sample holder. Data were collected from 5 to 40◦ 2 (step size = 0.026) at RT.

2.5.5. Chemical analysis

Fourier Transform Infrared Spectroscopy (FT-IR) spectra of the PLA and PLA bionanocomposite films were obtained at room temperature in reflection mode by attenuated total reflectance (ATR), with a FT-IR spectrometer (Jasco FT-IR 615, Japan). The scanned wavenumber range was 4000–600 cm−1 , at 4 cm−1 of spectral resolution.

2.5.6. Mechanical analysis

The mechanical response of PLA and PLA bionanocomposites was evaluated by tensile test according to the European Standard EN ISO 527-3:1995. Before testing, samples were conditioned at 22 ◦ C and 51%RH overnight. Experiments were carried out on a AGS-X Universal Testing Machine from Shimadzu at 5 mm/min by using 50 mm long and 10 mm width specimens. Young's modulus (E) (calculated from slope of a secant line between 0.5 and 1% strain on stress–strain plot), stress and strain at yield (y and εy respectively) and stress and strain at break (σb and εb respectively) were determined. Reported values represent mean average value and standard deviation over 5 specimens. Experimentally obtained tensile modulus could be compared with theoretical predictions by using a modified Halpin–Tsai model as (Halpin & Kardos, 1976; Hui & Shia, 1998):

$$\frac{E_c}{E_m} = \left(\frac{3}{8}\right)\left(\frac{1+2\rho\eta_L V_{CNC}}{1-\eta_L V_{CNC}}\right) + \left(\frac{5}{8}\right)\left(\frac{1+2\eta_T V_{CNC}}{1-\eta_T V_{CNC}}\right) \quad (4)$$

$$\eta_L = \frac{E_r - 1}{E_r + 2\rho} \quad \eta_T = \frac{E_r - 1}{E_r + 2} \quad (5)$$

where Ec and Em are the Young's modulus of the composite and matrix respectively, is the CNC aspect ratio, VCNC is its volume fraction within the bionanocomposite and ER is defined as the ratio between the Young's modulus of the filler and the matrix. CNC volume fractions have been calculated from the weight frac-tion of both components and their densities, assuming a density of 1.25 g/cm3 for PLA and 1.676 g/cm3 for cellulose nanocrystals (Diddens, Murphy, Krisch, & Muller, 2008), while the Young's mod-ulus of CNC-g-PLLA nanoparticles has been set at 105 GPa (Rusli & Eichhorn, 2008).

3. Results and discussions

3.1. CNC-g-PLLA nanohybrids characterization

Morphological, physico-chemical and conformational charac-terization of synthesized raw CNC and CNC-g-PLLA nanohybrids have been carried out as highlighted in Fig. 1. TEM micrograph shown in Fig. 1a presents rod-shaped well-individualized cellu-lose nanocrystals having a length of 150 ± 60 nm and width of about 9–17 nm (particle size distribution has been calculated from 8 TEM images). Conformational features of CNC grafted with PLLA were analyzed by FT-IR. Absorbance spectra corresponding to raw CNC, CNC-g-PLLA1 and CNC-g-PLLA2 are plotted in Fig. 1b, while the spectra of commercially available microcrystalline cellulose, l-lactide and medium molecular-weight poly(l-lactide) are provided for comparison (characteristic bands of cellulose, l-lactide and poly(l-lactide) are vertically expanded by a dashed line with , and X ends respectively). Synthesized CNC show the characteristic OH stretching vibration broad band at 3650–3200 cm−1 and a nar-rower band centered at 2902 cm−1 corresponding to the stretching of asymmetric and symmetric methyl and methylene C H groups (Kondo & Sawatari, 1996). Further bands assigned to the C O H in plane bending, C O C bending and C O C asymmetric stretch-ing at the B-(1 → 4)-glycosidic linkage are achieved at 1337 cm−1, 1160 cm−1 and 897 cm−1 respectively (Colom & Carrillo, 2002). A crystallinity degree of 52.9% is determined for employed CNC according to the A1431,1419 /(A1431,1419 + A897,894) ratio (Oh et al., 2005; Lizundia et al., 2015b). PLLA grafting on CNC surfaces is proved by the presence of the characteristic absorption bands of PLLA (CH3 group stretching at 3017 cm−1 , C O stretching vibration at 1760 cm−1 , in plane deformation at 1458 cm−1 , rocking vibration at 1187 cm−1) (Goncalves, Cuntinho, & Marrucho, 2010; Meaurio, Martinez de Arenaza, Lizundia, & Sarasua, 2009), together with the broad O H stretching band of cellulose for CNC-g-PLLA1 and CNC-g-PLLA2. Additionally, the relative 3650–3200 cm−1 (cellulose OH) and 1760 cm−1 (PLLA C O stretching) peak height indicates that the CNC-to-PLLA ratio is

significantly higher for CNC-g-PLLA1 nanohybrid. Results demonstrate that no traces of l-lactide remain in any of the synthesized nanohybrids.

Fig. 1c displays the heating differential scanning calorime-try traces for both CNC-g-PLLA1 and CNC-g-PLLA2 nanohybrids. Although CNC-g-PLLA1 does not suffer any thermal transition within the studied temperature range suggesting that a very small fraction of grafted PLLA, CNC-g-PLLA2 presents several thermal transitions associated with the glass transition (heat enthalpy change located at 47.8 ◦ C), cold crystallization (exothermic peak at 78.3 ◦ C) and melting of grafted PLLA chains (at 158 ◦ C) (Lizundia et al., 2013). The low Tg , Tcc and Tm values measured for CNC-g-PLLA2 evidence the low molecular weight of grafted chains for this nanohybrids (Lizundia, Meaurio, Laza, Vilas, & León, 2015a). Addi-tionally, the thermal stability of raw CNC and both synthesized nanohybrids, has been evaluated by thermogravimetric analysis under nitrogen atmosphere (TGA trace corresponding to l-lactide is shown as reference, Fig. 1d). Thermal degradation of raw CNC, which is due to the depolymerization, dehydration and decompo-sition of cellulosic glycosyl units (Roman & Winter, 2004) starts at 270.2 ◦ C and reaches its maximum value (Tmax) at 332.9 ◦ C. On the contrary, CNC-g-PLLA1 thermodegradation takes place at lower temperatures (Tmax = 311.6 ◦ C), while CNC-g-PLLA2 degrades at similar temperatures than raw CNC. The reduced thermal sta-bility of CNC-g-PLLA1 originates from the presence of residual tin compound arising from SI-ROP process, which boosts the thermod-egradation process of nanohybrids (Lizundia et al., 2015b). The amount of char residue at 400 ◦ C indicates that the CNC-to-PLLA ratio within nanohybrids is much larger in CNC-g-PLLA1 nanohy-brid in comparison with CNC-g-PLLA2.

3.2. PLA CNC-g-PLLA bionanocomposite films

3.2.1. Morphological analysis

Fig. 2 shows the FESEM images of the cryogenic fractured sur-faces of neat PLA and PLA based bionanocomposite films at different magnifications. Neat PLA showed a smooth and uniform surface typical of a semicrystalline polymer, as previously observed (Yang, Dominici, Fortunati, Kenny, & Puglia, 2015). A similar behavior was also observed for PLA 1CNC-g-PLLA1 bionanocomposites, underlin-ing a good dispersion of these cellulose nanocrystals in the polymer matrix. On the other hand, the surfaces of specimens with differ-ent content of CNC-g-PLLA2 showed a different microstructure: at lower concentration (1 wt.%) samples showed relatively small domains with a typical sea-island morphology, while increasing the CNC content (3 wt.%) some aggregates were evident.

3.2.2. Optical properties

Optical properties, UV–vis spectra, colorimetric analysis and gloss of the films are directly related with their nano- and micro-structure.

The transparency of the produced PLA based films was eval-uated by UV–vis optical absorption measurements, in the visible to reflect direct light. As can be seen, gloss values decreased with CNC introduction. The gloss of the films is linked to the morphology of their surface and to the dispersion and aggregation of nano-structure in the polymer matrix (Sonjui & Jiratumnukul, 2014). It is observed that PLA losses a gloss with the CNC addition. This effect is mainly evident with CNC-g-PLLA2, which should be expected due to the lactide units and CNC distribution. Gloss of both nanocom-posite films was significantly lower than neat PLA film. The CNC modifications made possible the retention of the high original gloss (∼129), while the increase of the CNC content dramatically reduce PLA gloss to 60.

3.2.3. Thermal properties

Differential scanning calorimetry was used to investigate the glass transition, crystallization and melting phenomena of PLA and PLA bionanocomposites and study the effect of CNC addition, grafting and content on the final properties of the produced PLA based formulations. DSC thermograms during first heating, cool-ing and second heating scan are shown in Fig. 3 while the thermal properties obtained during the first and second heating scans are summarized in Table 2. The glass transition temperatures, crystal-lization and melting phenomena of the bionanocomposites did not change significantly respect to the PLA polymer matrix during the first heating scan (Fig. 3a). Only the PLA 3CNC-g-PLLA2 formulation showed a shift to lower temperature of the Tcc1 of about 10 ◦ C with an increase in the crystallinity degree values (PLA = (12.8 ± 1.8)%, PLA 3CNC-g-PLLA2 = (18.6 ± 1.5)%) that underlined the effect of this graft type and the best efficiency of the highest content of CNC-g-PLLA2 (3 wt.%). The effectiveness of CNC-g-PLLA2 at 3 wt.% was also confirmed during the cooling scan were the crystallization phenomenon was evident for PLA 3CNC-g-PLLA2 formulation with an enthalpy value of (32.5 ± 2.3)J/g respect to the (3.2 ± 0.3)J/g of neat PLA. These results are in agreement with the WAXD analysis, as would be shown later. Finally, also during the second heating scan, the PLA 3CNC-g-PLLA2 bionanocomposite showed the high-est value of crystallinity degree (39.6%) while the different ability to re-crystallize after the cooling was highlighted by the low val-ues of the first cold crystallization enthalpy (Hcc1 = 6.7 J/g respect to 28.7 J/g of the neat PLA) and the absence of the second cold crystallization enthalpy registered for this system.

The analysis of thermodegradation products would give further insights on the occurring thermodegradation pathways. Accord-ingly, the normalized spectra (according to CO2 absorption band, 2362 cm−1) corresponding to exhaust gases obtained during the maximum rate of thermal degradation for raw CNC, CNC-g-PLLA1, CNC-g-PLLA2 and their PLA based bionanocomposite films are shown in Fig. 4. Fig. 4a shows the relative weight of PLA and the nanocomposites films based on CNC at different content. It is evi-dent that the CNC presence and content do not affect the thermal degradation behaviour. During thermodegradation of the neat PLA, methyl alcohol (broad band at 3150–2650 cm−1 and sharper one at 1100–950 cm−1), carbon monoxide (2176 cm−1 and 2120 cm−1), carbon dioxide (2362 cm−1 , 2334 cm−1

and 669 cm−1) and water were released (McNeill & Leiper, 1985; Zou, Yi, Wang, Liu, & Xu, 2009). On the contrary, as a result of cleavage of the glycosidic link-ages, the thermal degradation of raw CNC yields mainly CO2 , water (multiple peaks in between 1900–1300 cm−1), and CO compounds (Bourbigot, Chlebicki, & Mamleev, 2002).

The spectrum corresponding to CNC-g-PLLA1 is fairly similar to that obtained for raw CNC, while the CNC-g-PLLA2 thermod-egradation yields acetaldehyde (broad band at 2733 cm−1 and shaper ones at 1759 cm−1 , 1370 cm−1 and 1106 cm−1), CO2 , CO and water, which are characteristic of the thermal degradation of polylactides (McNeill & Leiper, 1985). Obtained spectra sug-gest that CNC-g-PLLA1 is mainly composed by cellulose, while CNC-g-PLLA2 presents large polylactide fractions. This difference results in rather different thermodegradation pathways of bio-nanocomposite films. In comparison with PLA 3CNC-g-PLLA1 bionanocomposite, the addition of 3 wt.% of CNC-g-PLLA2 to PLA matrix resulted in the development of larger quantities of CO (intensity increase of 2176 cm−1 and 2120 cm−1 peaks) and water. Both bionanocomposites released methyl alcohol and acetaldehyde during their thermodegradation (3200–2600 cm−1), although the presence of acetaldehyde was larger in the case of PLA 3CNC-g-PLLA2 as denoted by the increase in 2740 cm−1 band. Moreover, acetaldehyde/CO2 ratio (estimated from 2362/1759 ratio), shifted from 0.66 for PLLA CNC-g-PLLA1 to 1.3 for PLLA CNC-g-PLLA2 bio-nanocomposite. In overall, those changes could be attributed to the differences on the amount of grafted PLLA chains in CNC-g-PLLA1 and CNC-g-PLLA2 nanohybrids.

3.2.4. X-ray diffraction

Fig. 5a shows wide angle X-ray diffraction (WAXD) spectra of synthesized raw CNC, CNC-g-PLLA1, CNC-g-PLLA2 and their PLA based bionanocomposite films. It is observed that raw CNC presents three main peaks located at 15.7◦ , 22.5◦ and 35◦ corresponding to (1 0 1), (0 0 2) and (0 4 0) planes of CNC crystal lattice respec-tively (Park, Baker, Himmel, Parilla, & Johnson, 2010). It is important to emphasize that WAXD patterns of grafted CNC greatly differ from each other. While CNC-g-PLLA1 only showed the charac-teristic diffraction peaks corresponding to crystalline cellulose, CNC-g-PLLA2 showed featured reflections of PLLA orthorhombic form corresponding to (0 1 0), (1 1 0)/(2 0 0), (2 0 3) and (0 1 5) planes achieved at 2 = 14.8◦ , 16.8◦ , 19.2◦ and 22.3◦ , respectively (Kobayashi et al., 1995). Those data suggested that the presence of grafted PLLA chains in the synthesized CNC-g-PLLA1 was very low in comparison with CNC-g-PLLA2. Additionally, it resulted reason-able to suppose that the rather low molecular weight of PLLA chains in CNC-g-PLLA2 nanohybrid (as evidenced by its low melting tem-perature of 158 ◦ C) confers high crystallization ability to attached chains.

Although all fabricated bionanocomposite films presented a broad halo centered at 2 —16◦ denoting a predominantly amor-phous microstructure of specimens, its height slightly increased for

bionanocomposites containing 3 wt.% of both CNC-g-PLLA. This increased intensity was ascribed to the development of ordered regions during the filmature process, which agrees well with obtained DSC data where it is shown that the crystallinity degree increases from 12.8% for neat PLA to 18.6% for its PLA 3CNC-g-PLLA2 bionanocomposite (see Table 2). In order to confirm the presence of CNC within the fabricated films, further WAXD experiments were carried out for longer times. Fig. 5b displays obtained diffraction patterns for bionanocomposites containing 3 wt.% within the 2 = 8–28◦ region (neat CNC pattern is shown for comparison). It was observed that besides of the predominant main amorphous halo, both PLA 3CNC-g-PLLA1 and PLA 3CNC-g-PLLA2 bionanocomposites presented a small shoulder located at 2=22.5◦ corresponding to the (0 0 2) plane of CNC crystal lattice, which certified the presence of cellulosic crystals within the films.

3.2.5. Infrared spectroscopy

The FT-IR spectra of (c) PLA-CNC-g-PLLA1 and (d) PLA-CNC-g-PLLA2 films are presented in Fig. 5. This analysis attempts to characterize the incorporation of CNC-g-PLLA nanohybrids in PLA based films and distinguish the infrared bands and vibration shifts related to interactions. The absorption peaks of the bionanocom-posite spectrum were mainly due to the CH3 stretching vibration at 2990 cm−1 . A strong absorption band was observed at 1757 cm−1 due to the C O stretching from keto esters. The sample with CNC-g-PLLA1showed an increased absorption peak between 3300 and 3400 cm−1 due to the CNC presence in the film, as underlined in Fig. 1b. As the CNC-g-PLLA content was increased from 1 wt.% to 3 wt.%, the stretching vibrations of OH groups of cellulose increased gradually. Spectra showed the typical features of cellulose, the broad bands in the 3650–3000 cm−1 region are due to O H stretch-ing vibrations. The bending vibrations at 1452 and 1382 cm−1 were due to the antisymmetric and symmetric deformations of CH3 group, as already reported by Pamula, Błazewicz,˙ Paluszkiewicz, and Dobrzynski´ (2001) in the region 1300–1500 cm−1 . The bands at 1266 and 1189 cm−1 were related to the antisymmetric and symmetric stretching of COC in esters. The peak at 1181 cm−1 could be attributed to COC stretching of PLA (Molinaro et al., 2013).

3.2.6. Mechanical properties

Fig. 6 depicts the stress–strain curves of raw PLA and its bionanocomposites, while the main representative mechanical parameters are summarized in Table 1. Neat polymer presented a stiff and semi-ductile behaviour with a strain at yield (εy) of 2.6% and strain at break (εb) of 5.6%. As a general rule, tensile modulus was continuously increased at expenses of ductility upon CNC-g-PLLA nanohybrids loading. Those changes were especially noticeable for the PLA CNC-g-PLLA2 nanocomposites, where the Young's modulus increases by 23% with the addition of 3 wt.% of cellulose nanocrystals. Surprisingly, the elongation at break of PLA 1CNC-g-PLLA1 was increased from 5.6% up to 9.5%, which may be attributed to the increased

dispersion and interfacial adhesion provided by the grafted PLLA chains (Lönnberg, Larsson, Lindström, Hult, & Malmström, 2011; Lin, Chen, Huang, Dufresne, & Chang, 2009). More precisely, it has been previously suggested that grafted chains create a co-continuous phase in which local stresses are evenly transferred to the remaining PLA phase, which in turn improved the mechanical properties of the bulk material (Cao, Habibi, & Lucia, 2009).

Fig. 6b compares the experimentally obtained data and pre-dicted Young's modulus values according to random Halpin–Tsai equation. It is noticed that the experimental values remained below the predicted data, which is especially noticeable at high concentra-tions and for the PLA CNC-g-PLLA1 system. The fact that the Young's modulus of PLA 1CNC-g-PLLA2 (corresponding to a volume frac-tion of 0.75%) fits rather well may be ascribed to an effective stress transfer across the CNC-to-PLA interface together with a good CNC distribution over the entire bionanocomposite (Choudhury, 2014). However, it could be concluded from the overprediction of ten-sile modulus that other formulations yield a non-homogeneous aggregated morphology.

4. Conclusions

Cellulose nanocrystals were subjected to surface grafting of poly(l-lactide) through ring opening polymerization initiated from the hydroxyl groups available on their surface. The resulting CNC-g-PLLA nanohybrids were successfully incor-porated in poly(lactic acid) polymer matrix through melt-blending. The effect of cellulose modification and amount in the bionanocom-posites was deeply characterized in terms of their morphological, optical and thermo-mechanical properties. The CNC:l-lactide ratios affect the grafting efficiency and, con-sequently, the bionanocomposite thermal, mechanical and optical properties.

Microstructure analysis and optical properties underlined a good dispersion of cellulose nanocrystals in the polymer matrix. Thermal properties highlighted the best efficiency in the samples with the highest content of CNC-g-PLLA2 (3 wt.%). Tensile modulus was increased with the CNC introduction, as expected, while the elongation at break of PLA 1CNC-g-PLLA1 was improved of the 70% respect to PLA polymer matrix film.

Acknowledgements

E.L. thanks the University of the Basque Country (UPV/EHU) for a postdoctoral fellowship. We gratefully acknowledge Corbion-Purac for the kind donation of l-lactide monomer and PLLA. Technical and human support provided by SGIker (UPV/EHU, MICINN, GV/EJ, EGEF, and ESF) is gratefully acknowledged.

References

Arias, A., Heuzey, M. C., Huneault, M. A., Ausias, G., & Bendahou, A. (2015). Enhanced dispersion of cellulose nanocrystals in melt-processed polylactide-based nanocomposites. Cellulose, 22, 483–498.

Armentano, I., Bitnis, N., Fortunati, S., Rescignano, N., Verdejo, R., Lopez-Manchado, M. A., et al. (2013). Multifunctional nanostructured PLA materials for packaging and tissue engineering. Progress in Polymer Science, 38(10–11), 1720–1747.

Auras, R. Harte, & Selke, B. S. (2004). An overview of polylactides as packaging materials. Macromolecular Bioscience, 4, 835–864.

Bitinis, N., Verdejo, R., Bras, J., Fortunati, E., Kenny, J. M., Torre, L., et al. (2013). Poly(lactic acid)/natural rubber/cellulose nanocrystal bionanocomposites Part I. Processing and morphology. Carbohydrate Polymers, 96, 611–620.

Bourbigot, S., Chlebicki, S., & Mamleev, V. (2002). Thermal degradation of cotton under linear heating. Polymer Degradation and Stability, 78, 57–62.

Cao, X., Habibi, Y., & Lucia, L. A. (2009). One-pot polymerization, surface grafting, and processing of waterborne polyurethane-cellulose nanocrystal nanocomposites. Journal of Materials Chemistry, 19, 7137–7145.

Choudhury, A. (2014). Preparation and characterization of nanocomposites of poly-p-phenylene benzobisthiazole with graphene nanosheets. RSC Advances, 4, 8856–8866.

CIE. (1995). Industrial colour-difference evaluation. In Technical report 116/1995 (1995 ed.). Wien, Austria: Commission Internationale de I'Eclairage Central Bureau.

Colom, X., & Carrillo, F. (2002). Crystallinity changes in lyocell and viscosetype fibres by caustic treatment. European Polymer Journal, 38, 2225–2230.

Dechy-Cabaret, O., Martin-Vaca, B., & Bourissou, D. (2004). Controlled ring-opening polymerization of lactide and glycolide. Chemical Reviews, 104, 6147–6176. Diddens, I., Murphy, B., Krisch, M., & Muller, M. (2008). Anisotropic elastic properties of cellulose measured using inelastic X-ray scattering. Macromolecules, 41, 9755–9759.

Dufresne, A. (2013). Nanocellulose: A new ageless bionanomaterial. Materials Today, 16, 220–227.

Fortunati, E., Armentano, I., Zhou, Q., Iannoni, A., Saino, E., Visai, L., et al. (2012). Multifunctional bionanocomposite films of poly(lactic acid), cellulose nanocrystals and silver nanoparticles. Carboydrate Polymers, 87, 1596–1605.

Fortunati, E., Armentano, I., Zhou, Q., Puglia, D., Terenzi, A., Berglund, L. A., et al. (2012). Microstructure and nonisothermal cold crystallization of PLA composites based on silver nanoparticles and nanocrystalline cellulose. Polymer Degradation and Stability, 97, 2027–2036.

Goffin, A. L., Raquez, J. M., Duquesne, E., Siqueira, G., Habibi, Y., Dufresne, A., et al. (2011). From interfacial ring-opening polymerization to melt processing of cellulose nanowhisker filled polylactide based nanocomposites. Biomacromolecules, 12, 2456–2465.

Goncalves, C. M. B., Cuntinho, J. A. P., & Marrucho, I. M. (2010). In R. A. Auras, L. T. Lim, & S. E. M. Selke, et al. (Eds.), Poly(lactic acid): Synthesis, structures, properties, processing and applications (pp. 97–112). Hoboken, NJ: John Wiley & Sons Inc.

Habibi, Y., Aouadi, S., Raquez, J. M., & Dubois, P. (2013). Effects of interfacial stereocomplexation in cellulose nanocrystal-filled polylactide nanocomposites. Cellulose, 20, 2877–2885.

Habibi, Y. (2014). Key advances in the chemical modification of nanocelluloses. Chemical Society Reviews, 43, 1519.

Halpin, J. C., & Kardos, J. L. (1976). The Halpin–Tsai equations: A review. Polymer Engineering and Science, 16, 344–352.

Hui, C. Y., & Shia, D. (1998). Simple formulae for the effective moduli of unidirectional aligned composites. Polymer Engineering and Science, 38, 774–782.

Kobayashi, J., Asahi, T., Ichiki, M., Oikawa, A., Suzuki, H., Watanbe, T., et al. (1995). Structural and optical properties of poly lactic acids. Journal of Applied Physiscs, 77, 2957–2973.

Kondo, T., & Sawatari, C. (1996). A Fourier transform infrared spectroscopic analysis of the character of hydrogen bonds in amorphous cellulose. Polymer, 37, 393–399.

Lin, N., Chen, G., Huang, J., Dufresne, A., & Chang, P. R. (2009). Effects of polymergrafted natural nanocrystals on the structure and mechanical properties of poly(lactic acid): A case of cellulose whisker-graft polycaprolactone. Journal of Applied Polymer Science, 113(5), 3417–3425.

Liu, G., Zhang, X., & Wang, D. (2014). Tailoring crystallization: Towards high-performance poly(lactic acid). Advanced Materials, 26(40), 6905–6911.

Lizundia, E., Petisco, S., & Sarasua, J. R. (2013). Phase-structure and mechanical properties of isothermally melt-and cold-crystallized poly(l-lactide). Journal of the Mechanical Behavior of Biomedical Materials, 17, 242–251.

Lizundia, E., Meaurio, E., Laza, J. M., Vilas, J. L., & León, L. M. (2015). Study of the chain microstructure effects on the resulting thermal properties of poly(l-lactide)/poly(N-isopropylacrylamide) biomedical materials. Materials Science and Engineering C: Materials for Biological Applications, 50, 97–106.

Lizundia, E., Vilas, J. L., & León, L. M. (2015). Crystallization, structural relaxation and thermal degradation in poly(l-lactide)/cellulose nanocrystal renewable nanocomposites. Carbohydrate Polymers, 123, 256–265.

Lönnberg, H., Larsson, K., Lindström, T., Hult, A., & Malmström, E. (2011). Synthesis of polycaprolactone-grafted microfibrillated cellulose for use in novel bionanocomposites-influence of the graft length on the mechanical properties. ACS Applied Materials and Interfaces, 3(5), 1426–1433.

Martin, O., & Avérous. (2001). Poly(lactic acid): Plasticization and properties of biodegradable multiphase systems. Polymer, 42(14), 6209–6219.

McNeill, I. C., & Leiper, H. A. (1985). Degradation studies of some polyesters and polycarbonates-1. Polylactide: General features of the degradation under programmed heating conditions. Polymer Degradation and Stability, 11, 267–285.

Meaurio, E., Martinez de Arenaza, I., Lizundia, E., & Sarasua, J. R. (2009). Analysis of the C O stretching band of the -crystal of Poly(l-lactide). Macromolecules, 42, 5717–5727.

Molinaro, S., Romero, M. C., Boaro, M., Sensidoni, A., Lagazio, C., Morris, M., et al. (2013). Effect of nanoclay-type and PLA optical purity on the characteristics of PLA-based nanocomposite films. Journal of Food Engineering, 117, 113–123.

Obarzanek-Fojt, M., Elbs-Glatz, Y., Lizundia, E., Diener, L., Sarasua, J. R., & Bruinink, A. (2014). From implantation to degradation—Are poly(l-lactide)/multiwall carbon nanotube composite materials really cytocompatible? Nanomedicine: Nanotechnology, Biology and Medicine, 10(5), 1041–1051.

Oh, S. Y., Yoo, D. I., Shin, Y., Kim, H. C., Kim, H. Y., Chung, Y. S., et al. (2005). Crystalline structure analysis of cellulose treated with sodium hydroxide and carbon dioxide by means of X-ray diffraction and FTIR spectroscopy. Carbohydrate Research, 340, 2376–2391.

Pamula, E., Błazewicz,˙ M., Paluszkiewicz, C., & Dobrzynski,´ P. (2001). FTIR study of degradation products of aliphatic polyesters–carbon fibres composites. Journal of Molecular Structure, 596, 369–375.

Park, S., Baker, J. O., Himmel, M. E., Parilla, P. A., & Johnson, D. K. (2010). Cellulose crystallinity index: Measurement techniques and their impact on interpreting cellulase performance. Biotechnology for Biofuels, 3, 10.

Paul, D. R., & Robeson, L. M. (2008). Polymer nanotechnology: Nanocomposites. Polymer, 49(15), 3187–3204.

Roman, M., & Winter, W. T. (2004). Effect of sulfate groups from sulfuric acidhydrolysis on the thermal degradation behavior of bacterial cellulose. Biomacromolecules, 5, 1671–1677.

Rusli, R., & Eichhorn, S. J. (2008). Determination of the stiffness of cellulose nanowhiskers and the fiber–matrix interface in a nanocomposite using Raman spectroscopy. Applied Physics Letters, 93, 033111.

Song, Z., Xiao, H., & Zhao, Y. (2014). Hydrophobic-modified nano-cellulose fiber/PLA biodegradable composites for lowering water vapor transmission rate (WVTR) of paper. Carbohydrate Polymers, 111, 442–448.

Sonjui, T., & Jiratumnukul. (2014). Poly(lactic acid) organoclay nano composites for paper coating applications. Songklanakarin Journal of Science and Technology, 536(5), 535–540, 36.

Spinella, S., Lo Re, G., Liu, B., Dorgan, J., Habibi, Y., Leclere, P., et al. (2015). Polylactide/cellulose nanocrystal nanocomposites: Efficient routes for nanofiber modification and effects of nanofiber chemistry on PLA reinforcement. Polymer, 65, 9–17.

Turhan, K. N., & Sahbaz, F. (2001). A simple method for determining light transmittance of polymer films used for packaging foods. Polymer International, 50, 1138.

Xiao, S., Gao, R., Lu, Y., Li, L., & Sun, Q. (2015). Fabrication and characterization of nanofibrillated cellulose and its aerogels from natural pine needles. Carbohydrate Polymers, 119, 202–209.

Yang, W., Dominici, F., Fortunati, E., Kenny, J. M., & Puglia, D. (2015). Melt free radical grafting of glycidyl methacrylate (GMA) onto fully biodegradable poly(lactic) acid films: Effect of cellulose nanocrystals and a masterbatch process. RSC Advances, 5, 32350–32357.

Zou, H., Yi, C., Wang, L., Liu, H., & Xu, W. (2009). Thermal degradation of poly(lactic acid) measured by thermogravimetry coupled to Fourier transform infrared spectroscopy. Journal of Thermal Analysis and Calorimetry, 97, 929–935.

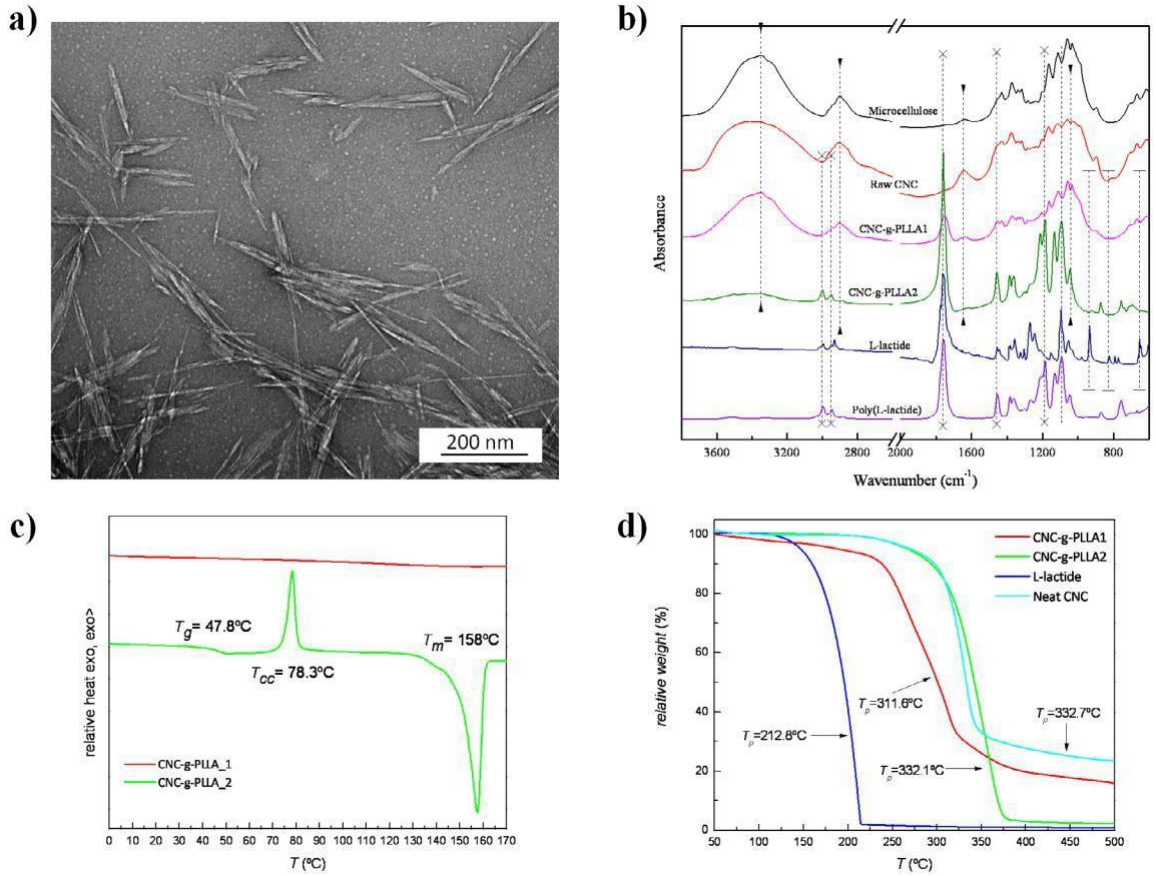

Fig. 1. (a) TEM image showing synthesized cellulose nanocrystals; (b) FT-IR spectra of neat CNC and CNC-g-PLLA nanohybrids; (c) DSC traces obtained after quenching samples from the melt of synthesized CNC-g-PLLA nanohybrids and (d) TGA of raw CNC and CNC-g-PLLA.

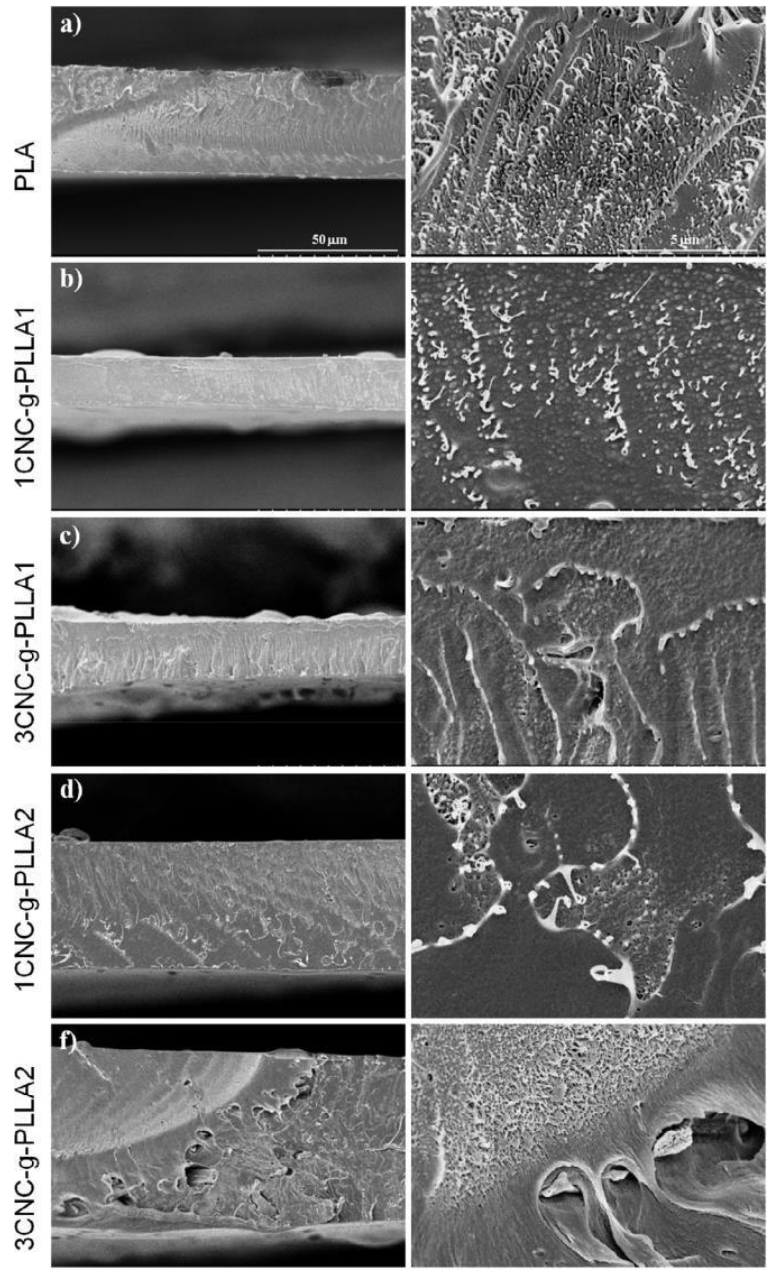

Fig. 2. FESEM micrographs of cryogenically fractured surfaces of PLA and PLA bionanocomposites: (a) PLA; (b) PLA 1CNC-g-PLLA1; (c) PLA 3CNC-g-PLLA1; (d) PLA 1CNC-g-PLLA2 and (e) PLA 3CNC-g-PLLA2.

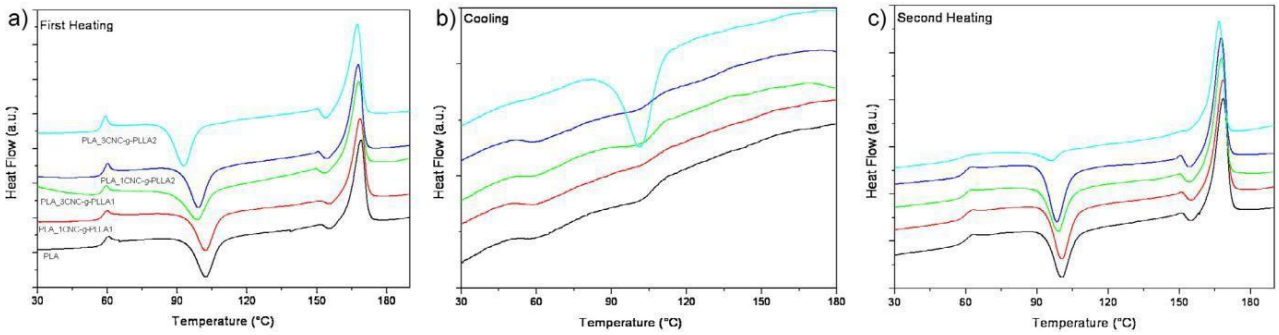

Fig. 3. DSC traces of neat PLA and its bionanocomposites obtained during: (a) first heating scan; (b) cooling from the melt and (c) second heating scan.

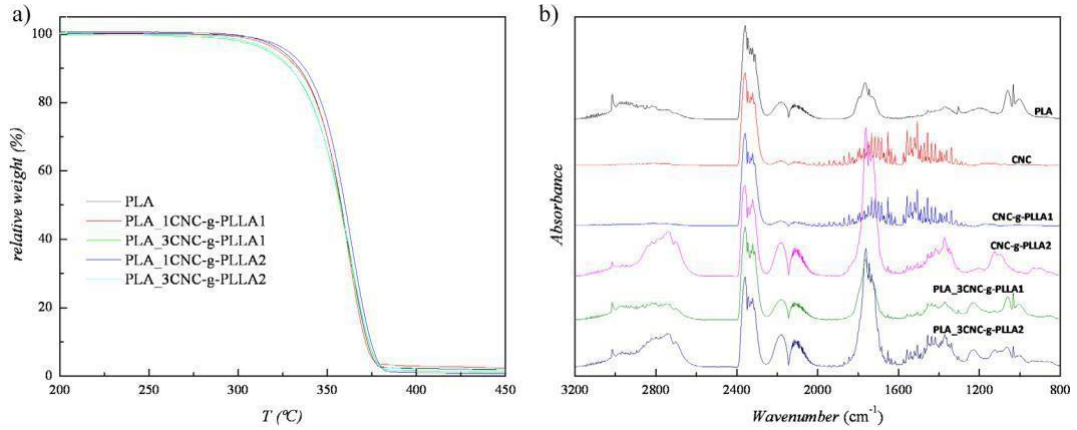

Fig. 4. (a) Thermogravimetric traces of neat PLA and its bionanocomposite counterparts and (b) FT-IR spectra of thermodegradation products obtained at the maximum weight loss.

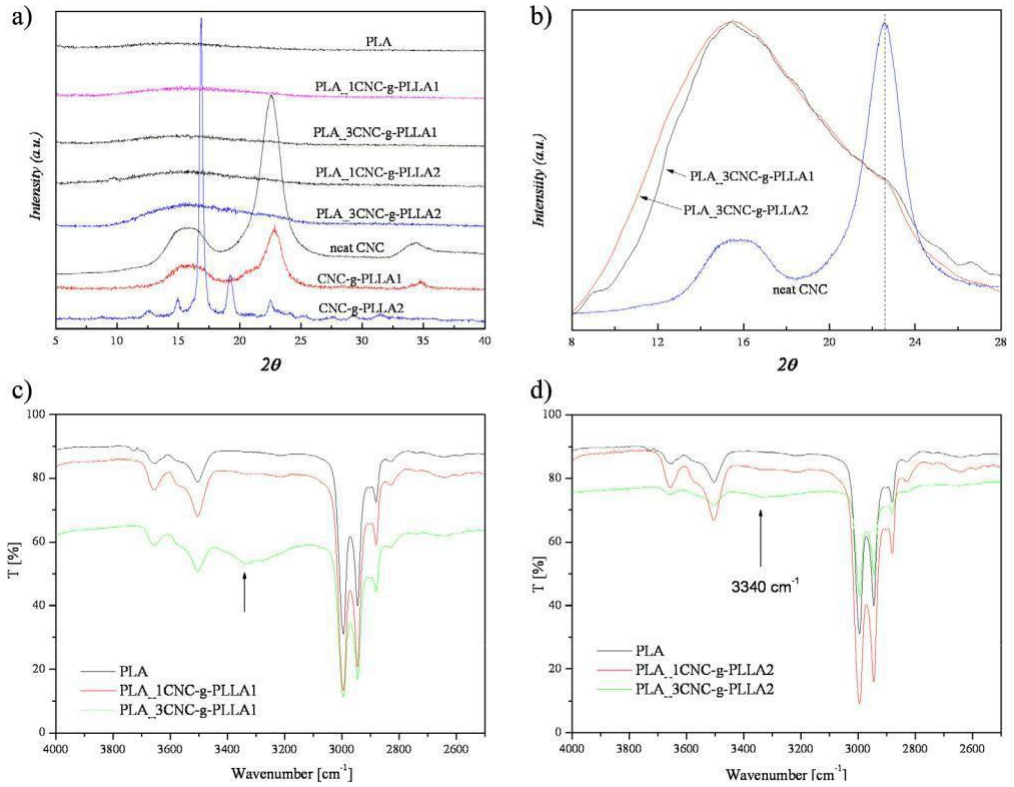

Fig. 5. (a) XRD patterns of synthesized CNC, CNC-g-PLLA nanosystems and its 1 wt.% and 3 wt.% nanocomposite counterparts and (b) enlarged XRD patterns within the 2 8–28◦ region. FT-IR spectra of (c) PLA CNC-g-PLLA1 and (d) PLA CNC-g-PLLA2 films.

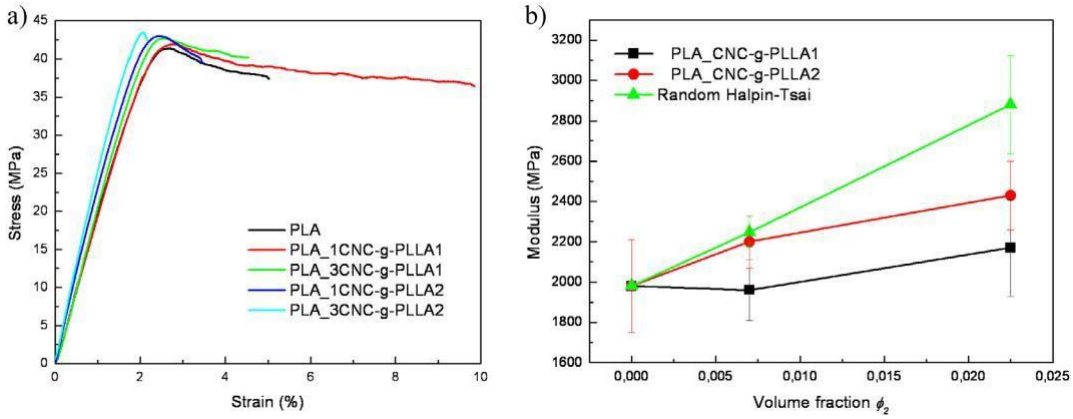

Fig. 6. (a) Representative stress–strain diagrams of neat PLA and PLA bionanocomposites and (b) experimental data and fitting results of neat PLA and PLA CNC-g-PLLA bionanocomposites.

Table 1: Apparent color, gloss and mechanical properties of PLA and PLA bionanocomposite films.

Formulations	L*	a*	b*	E*	Gloss	E (MPa)	ε_y (%)	$_y$ (MPa)	ε_b (%)	$_b$ (MPa)
PLA	93.57 ± 0.09	3.86 ± 0.08	15.76 ± 0.09	-	137	± 51980 ± 230	2.6 ± 0.1	41 ± 7	5.6 ± 0.6	37 ± 8
PLA 1CNC-g-PLLA1	93.04 ± 0.06	3.70 ± 0.08	14.86 ± 0.08	1.1 ± 0.1	124	± 51960 ± 150	2.8 ± 0.2	41.9 ± 1.4	9.5 ± 0.9	36 ± 4
PLA 3CNC-g-PLLA1	92.93 ± 0.09	3.62 ± 0.08	14.09 ± 0.08	1.8 ± 0.1	65 ± 6	2170 ± 240	2.5 ± 0.1	43 ± 4	4.4 ± 0.4	40 ± 4
PLA 1CNC-g-PLLA2	93.30 ± 0.20	3.83 ± 0.08	15.4 ± 0.4	0.5 ± 0.3	85 ± 9	2200 ± 130	2.4 ± 0.1	43 ± 6	3.4 ± 0.5	37.5 ± 1.6
PLA 3CNC-g-PLLA2	95.56 ± 0.06	3.58 ± 0.08	13.74 ± 0.08	2.3 ± 0.1	96 ± 7	2430 ± 170	2.1 ± 0.2	43.5 ± 1.5	2.2 ± 0.3	37.6 ± 1.5

Table 2: Thermal properties from DSC analysis of PLA and PLA bionanocomposite films from the first and the second heating scan.

Formulations	T_g (°C)	H_{cc1} (J/g)	T_{cc1} (°C)	H_{cc2} (J/g)	T_{cc2} (°C)	H_m (J/g)	T_m (°C)	X_c (%)
	First heating scan							
PLA	58.7 ± 0.7	32.5 ± 3.2	102.6 ± 0.3	1.6 ± 0.2	156.3 ± 0.5	46.1 ± 3.2	169.1 ± 0.6	12.8 ± 1.8
PLA 1CNC-g-PLLA1	58.6 ± 2.3	32.6 ± 0.7	101.8 ± 0.8	1.7 ± 0.1	156.3 ± 0.1	45.9 ± 0.1	168.4 ± 1.2	12.6 ± 0.6
PLA 3CNC-g-PLLA1	57.6 ± 0.8	31.6 ± 0.8	99.0 ± 1.0	3.0 ± 0.1	154.6 ± 0.5	48.6 ± 0.5	168.7 ± 0.9	15.6 ± 0.2
PLA 1CNC-g-PLLA2	58.8 ± 0.5	34.2 ± 0.3	99.1 ± 0.1	3.4 ± 0.3	154.2 ± 0.4	48.8 ± 0.3	168.3 ± 0.4	12.2 ± 0.4
PLA 3CNC-g-PLLA2	57.1 ± 0.3	32.0 ± 0.8	92.5 ± 0.3	3.3 ± 0.2	153.2 ± 0.3	51.8 ± 0.5	167.0 ± 0.8	18.6 ± 1.5
	Second heating scan							
PLA	60.4 ± 0.4	28.7 ± 2.3	100.5 ± 0.5	2.4 ± 0.3	15.8 ± 0.7	46.2 ± 0.3	168.7 ± 0.4	16.3 ± 2.4
PLA 1CNC-g-PLLA1	59.9 ± 0.3	29.0 ± 0.3	100.5 ± 0.2	2.3 ± 0.1	154.0 ± 0.1	47.9 ± 1.0	167.6 ± 0.7	18.1 ± 0.8
PLA 3CNC-g-PLLA1	59.8 ± 1.0	28.8 ± 0.7	99.2 ± 1.1	1.9 ± 0.1	153.2 ± 0.1	47.9 ± 0.5	168.8 ± 0.6	19.1 ± 0.1
PLA 1CNC-g-PLLA2	60.3 ± 0.3	32.0 ± 0.1	98.6 ± 0.3	3.3 ± 0.5	154.9 ± 0.1	50.4 ± 0.1	168.0 ± 0.1	16.4 ± 0.4
PLA 3CNC-g-PLLA2	57.7 ± 1.3	6.7 ± 0.7	96.2 ± 0.9	–	–	42.4 ± 0.7	166.0 ± 0.4	39.6 ± 0.7